Surface & Coatings Technology 496 (2025) 131643

Contents lists available at ScienceDirect

Surface & Coatings Technology

journal homepage: www.elsevier.com/locate/surfcoat

Investigating the influence of B, C, and N on the tribo-mechanical properties of the chemically complex TiSiBCN thin films using design of experiments

Wolfgang Tillmann [a], Julia Urbanczyk [a,*], Ahmad Zahid Ebady [a], Alexander Thewes [b], Günter Bräuer [b], Nelson Filipe Lopes Dias [a]

[a] Institute of Materials Engineering, TU Dortmund University, Leonhard-Euler-Straße 2, 44227 Dortmund, Germany
[b] Institute for Surface Technology, TU Braunschweig, Field Office Dortmund, Eberhardstr. 12, 44145 Dortmund, Germany

ARTICLE INFO

Keywords:
TiSiBCN
Design of Experiments
Nanocomposite
Magnetron sputtering

ABSTRACT

TiSiBCN thin films show promising properties like high hardness and improved tribological behavior. Adjusting the chemical composition can tailor the properties of these thin films. To investigate this influence, usually one element is varied. However, the interplay and influence of especially the light elements B, C, and N on the tribo-mechanical properties of chemical complex TiSiBCN thin films remain unclear. Therefore, a design of experiment using a central composite design (CCD) was employed to investigate the influences of these light elements on the tribo-mechanical properties of TiSiBCN thin films. TiSiBCN with varying chemical compositions were grown in a magnetron sputtering process by adjusting the cathode power of TiB_2/$TiSi_2$ composite targets and the gas flow rates of C_2H_2 and N_2.

X-ray diffraction (XRD) analysis revealed crystalline phases based on Ti, TiN, TiC, and TiB, with varying degrees of crystallinity dependent on the chemical composition, where the TiSiBCN thin films demonstrate a broad spectrum of mechanical properties, with hardness and elastic modulus ranging from 20.2 to 39.7 GPa and from 222.3 to 405.0 GPa, respectively. Notably, the B content significantly affects the mechanical properties, with the highest hardness and elastic modulus observed at 46.0 at.-% B. In tribometer tests against an Al_2O_3 ball under dry friction at room temperature, the TiSiBCN thin films also exhibit a broad spectrum of tribological properties, with the coefficients of friction (CoF) between 0.62 and 0.89 and wear rates between 6.4×10^{-5} and 12.2×10^{-5} mm^3/Nm. The lowest CoF of 0.62 with a wear rate of 7.7×10^{-5} mm^3/Nm is obtained for TiSiBCN with high amounts of 31.1 at.-% C and 33.5 at.-% N, while high 31.7 at.-% C and low 11.2 at.-% N contents favor the lowest wear rate of 6.4×10^{-5} mm^3/Nm with a CoF of 0.74. The tribological results reveal the significant influence of C and N on friction and wear, with TiSiBCN displaying reduced friction and wear tending to have lower hardness. Consequently, TiSiBCN thin films with either high hardness or enhanced friction and wear performance are attainable by adjusting the chemical composition.

Depending on the application requirements, the content of the light elements is decisive for the properties of TiSiBCN thin films. The CCD provides insights into the intricate interplay between the chemical composition and tribo-mechanical performance of TiSiBCN. Adjusting the concentrations of B, C, and N within TiSiBCN is crucial for tailoring the tribo-mechanical behavior to meet the specific requirements of applications.

1. Introduction

In forming processes, the tools are exposed to high mechanical and tribological loads. Thin films with high hardness, toughness, low friction, and improved wear properties can be used to extend the service life of these tools [1,2]. Tailored thin film systems are used to counteract specific load conditions. Depending on the range of abrasive and mechanical stresses, thin films based on nitrides and carbides are commonly used [1–4]. Amorphous carbon and boride-based thin films are suitable for reducing the tendency of workpiece material to adhere to the tool [3,5,6]. To effectively meet the growing demands on forming tools and enhance thin film properties in high-loaded forming processes,

* Corresponding author.
E-mail address: julia.urbanczyk@tu-dortmund.de (J. Urbanczyk).

https://doi.org/10.1016/j.surfcoat.2024.131643
Received 25 July 2024; Received in revised form 29 October 2024; Accepted 6 December 2024
Available online 10 December 2024

complex TiN-based nanocomposites with additions of C, Si, and B are gaining attention in research.

The established TiCN as a thin film forms a solid solution of TiC and TiN and combines the advantages and properties of both materials. TiCN thin films are characterized by a higher hardness and fracture toughness, enhanced chemical and thermal stability, reduced coefficient of friction (CoF), along favorable wear and abrasion resistance [7–9].

The addition of Si to TiN results in a nanocomposite structure with crystalline TiN embedded in an amorphous Si_3N_4 phase [10,11]. Patscheider et al. demonstrated that the Si enrichment leads to a reduction in TiN crystallite size following Hall-Petch theory and a favorable proportion of amorphous and crystalline phases the hardness of TiSiN thin film reached its maximum with 40 GPa at approximately 10 at.-% Si [11]. Furthermore, the a-Si_3N_4 phase acts as an oxidation barrier and protects the nc-TiN against oxidation up to 900 °C, even though TiN itself oxidizes at 500 °C [12].

The incorporation of B into TiCN combines the favorable tribo-mechanical properties of TiCN with a high hardness of $H > 40$ GPa and thermal stability of TiBN [13]. The chemical composition determines the formation of a nanocomposite, containing Ti(C,N) and Ti(B,C) crystals embedded in an amorphous matrix of a-C, a-CN, a-BN, and a-BC [14,15]. The hardness in this nanocomposite system increases following Hall-Petch relationship and is influenced by the proportions of amorphous to crystalline phases, which can be controlled by the N, C, and B contents. TiBCN thin films exhibit a high hardness up to 50 GPa, achieved with a N content of <8 at.-% due to the growth inhibition of crystallites. However, this comes at the expense of increased brittleness and a higher CoF of $\mu \approx 0.6$–0.7. A further rise of the N content leads to the substitution of B in the Ti(B,C) crystal lattice transforming into a Ti(N,C) lattice, while B forms an a-BN phase. This results in a reduction of hardness to 32 GPa for 15 at.-% N, but simultaneously, an increased amount of amorphous phases enhances toughness and improves tribological properties [14]. Increasing the C content in TiBCN thin films contributes to enhanced hardness due to the interstitial incorporation of the C atoms in the TiN lattice, causing lattice distortion. However, with a further increase in the amount of C, after filling all vacancies in the TiN lattice, additional a-C is formed, resulting in a hardness decrease [14,16]. Therefore, the CoF and wear rate are reduced due to the presence of self-lubricating a-C phases [17]. In a B variation of TiBCN thin films, the hardness increased from 22 GPa for TiCN to 42 GPa for thin films with a B content of 9 at.-%, attributed to crystallite refinement. Nevertheless, with a further rise in the B content, a decrease in hardness is observed as a result of a growing proportion of softer a-BN. The lowest friction of 0.52 was found at the lowest B content of 9 at.-% due to the higher amount of crystalline TiCN phases and the self-lubricating properties of a-C [18].

The addition of Si into TiBCN enhances oxidation resistance through the additional formation of a-Si_3N_4 phases [19]. The development of the complex quintenary TiSiBCN aims to combine the favorable tribo-mechanical properties of TiBCN and the thermal stability of TiSiN. TiSiBCN consists of phases of nc-(Ti,C,N)B_2 and nc-Ti(C,N) embedded in various amorphous phases, mainly a-Si_3N_4, a-$TiSi_2$ and a-SiC but also a-C, a-SiB_4, a-BN and a-CN_x [19,20]. By varying the N_2 flow rate in a PECVD process, TiSiBCN thin films reached a hardness up to 40 GPa with a relatively low N content of 9.4 at.-%, while maintaining oxidation resistance up to 750 °C across all films with varying N concentrations [19].

The previously mentioned studies demonstrate that the mechanical properties and tribological behavior of TiSiBCN thin films can be adjusted by certain content levels of either B, C, and N. It has also been shown that there is an interplay between B, C, and N which influences the characteristics of the developed phases within this complex quinternary TiSiBCN nanocomposite system and therefore its properties. Previous investigations only focused on varying one element of the chemical composition at a time, mainly N [19]. However, the interplay between the composition, phase development, and resulting tribo-mechanical properties is more complex and has not been investigated yet. This study addresses this gap by varying B, C, and N in a Design of Experiments (DoE) approach to provide an understanding of their interaction effect on the tribo-mechanical properties of TiSiBCN thin films.

2. Experimental setup

2.1. Deposition process

The TiSiBCN thin films were deposited using an industrial magnetron sputtering device CC800/9 Custom (CemeCon AG, Germany) which is schematically shown in Fig. 1. One Ti target, one $Ti_{80}Si_{20}$ target (ratio of 80/20 at.-%) and two $TiB_2/TiSi_2$ targets (ratio of 80/20 mol.-%) (Plansee Composite Material GmbH, Germany) were mounted on the magnetron cathodes. The rectangular-shaped targets had an area of 88 × 500 mm^2. Cylindrical discs of the high-speed steel (AISI M2) with a diameter of 30 mm, a thickness of 5 mm, and a hardness 60 HRC as well as n-type Si(100) wafers with a dimension of 10 × 50 mm^2 served as substrate material and were ultrasonicly cleaned in ethanol for 15 min. The deposition chamber was evacuated to a base pressure below 5 mPa. The deposition chamber has a size of 850 × 850 × 1.000 mm^3, the deposition room exhibits a diameter of 400 mm and a height of 400 mm. The distance between the target and substrate was approximately 170 mm. Before deposition, the substrates were etched by Ar^+ ions at a pulsed bias voltage (BV) of $U_b = -650$ V with a mid-frequency (mf) of $f = 350$ kHz for $t = 30$ min. In the first deposition step, a metallic 200 nm Ti layer was sputtered from the Ti target at a cathode power of $P_c = 4$ kW and a direct current bias voltage (dc-BV) of $U_b = -100$ V in an Ar-regulated pressure of $p = 350$ mPa. The second TiN layer with 300 nm thickness was applied by adding a N_2 gas flow of $q_{N2} = 70$ sccm in a N_2-regulated pressure of $p = 350$ mPa. The next 500 nm TiSiN interlayer was deposited from the $Ti_{80}Si_{20}$ targets with a dc-BV of $U_b = -100$ V. The Ti/TiN/TiSiN interlayer structure was applied to improve the adhesion to the steel substrate [21]. For the deposition of the functional TiSiBCN thin films a design of experiment (DoE) was carried out. The cathode power P_c of the two $TiB_2/TiSi_2$ targets, as well as the reaction gas flow rates of acetylene (C_2H_2) q_{C2H2} and N_2 q_{N2} were varied according to the experimental CCD plan (see Fig. 2 and Table 1). The two cathodes were operated in mf of $f_c = 50$ kHz and a BV of $U_b = -100$ V with a mf of $f = 350$ kHz. The process pressure was controlled by the Ar gas flow to $p = 350$ mPa. The deposition time was set to 4800 s for all TiSiBCN thin films.

2.2. Design of experiment (DoE)

To systematically analyze the influence of the B, C, and N contents on the properties of TiSiBCN thin films, the three parameters ($k = 3$)

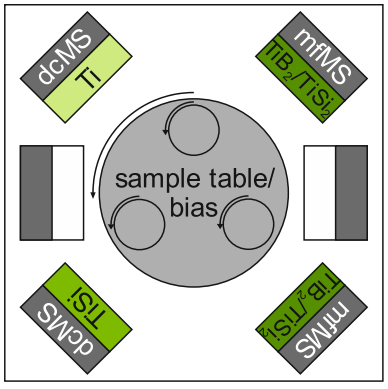

Fig. 1. Magnetron sputtering set up for the deposition of Ti/TiN/TiSiN interlayer system and TiSiBCN top layer in a DoE variation.

Factor k			Factor levels		
Cathode power	P_c	(kW)	3	4	5
Acetylene (C_2H_2) gas flow rate	q_{C2H2}	(sccm)	5	12.5	20
Nitrogen (N_2) gas flow rate	q_{N2}	(sccm)	10	40	70

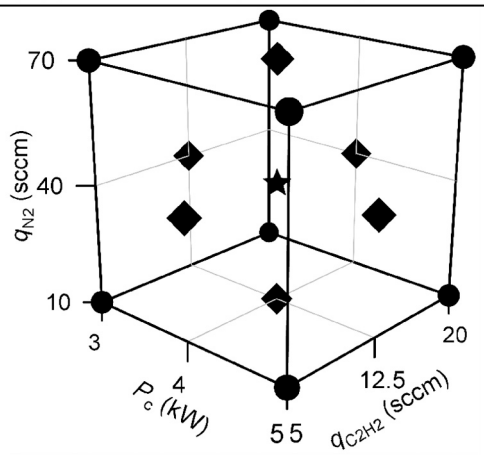

Fig. 2. Factor levels of the factors cathode power P_c of the $TiB_2/TiSi_2$ cathodes, C_2H_2 flow rate $q_{C2H2,}$ N_2 flow rate q_{N2}, and the resulting experimental CCD layout with central point $2^k + 2\bullet k + n_0$.

cathode power P_c of the $TiB_2/TiSi_2$ targets, C_2H_2 flow rate $q_{C2H2,}$ and N_2 flow rate q_{N2} were varied in three levels (see Fig. 2). The DoE was carried out using a face-centered central composite design (CCD) with a central point ($n_0 = 1$) to determine additional non-linear factors (see Fig. 2). A total of 15 experiments were conducted, with eight corner points (2^k), six star points ($2\bullet k$) and one central point (n_0). The 15 runs with the respective parameter settings can be found in Table 1. The experimental plan for the DoE was generated and analyzed using the statistical software JMP (SAS Institute Inc., USA) with a significance level of $\alpha = 0.02$. The statistical significance is visualized by a Pareto diagram when the so-called t value crosses the significance level α.

Concerning the use of TiSiBCN thin films for tool applications, based on the DoE an optimization was carried out. Therefore hardness H, the elastic modulus E, and the adhesion behavior L_{c3} have to be maximized, whereas the CoF μ and the wear rate k have to be minimized and were given all the same weighting of 0.2.

2.3. Characterization of the thin films

The chemical composition of the TiSiBCN thin films was quantitatively determined using an electron probe microanalyzer (EPMA) equipped with four wavelength-dispersive X-ray spectroscopy (WDS). The acceleration voltage was set to 10 keV at a beam current of 20 nA. The counting times were 10 s for the peak and 5 s for the background signal. The beam diameter was 5 μm. The analysis of the crystalline phases of the multilayered thin films was carried out with X-ray diffraction (XRD) at the beamline BL9 of the synchrotron light source DELTA (TU Dortmund University, Germany) [22]. The photon energy was set to 27 keV and a beamsize of 0.7 mm width and 0.1 mm height was used. The angle of incidence was set to 0.5° and an image plate detector (MAR345) was utilized for detection of the diffraction images. The microstructure and surface morphology of the thin film systems were analyzed by scanning electron microscopy (SEM) in secondary electron (SE) mode. The residual stresses were determined from the substrate curvature using Stoney's equation [23]. For this purpose, the curvature radius of the coated n-type Si(100) wafers was measured with

Table 1
DoE parameter settings, chemical composition, and deposition rate of the TiSiBCN thin films

Run	DoE parameter			Chemical composition (at.-%)							Deposition rate (nm/s)
	P_c (kW)	q_{C2H2} (sccm)	q_{N2} (sccm)	Ti	Si	B	C	N	O	Ar	
1	3	5	10	23.12 ± 0.46	8.69 ± 0.09	44.24 ± 0.44	6.42 ± 0.07	14.37 ± 0.17	2.59 ± 0.10	0.71 ± 0.01	0.17
2	5	5	10	26.20 ± 0.79	9.07 ± 0.09	46.04 ± 0.65	3.89 ± 0.23	11.61 ± 0.24	2.59 ± 0.17	0.59 ± 0.02	0.26
3	3	20	10	18.81 ± 0.26	6.82 ± 0.18	27.67 ± 0.25	31.70 ± 0.36	11.16 ± 0.30	2.41 ± 0.08	1.43 ± 0.03	0.18
4	5	20	10	22.11 ± 0.55	8.36 ± 0.14	36.68 ± 0.33	19.28 ± 0.27	10.27 ± 0.23	2.38 ± 0.36	0.92 ± 0.03	0.24
5	3	5	70	17.68 ± 0.54	6.41 ± 0.14	22.3 ± 0.12	8.99 ± 0.23	40.55 ± 0.40	2.17 ± 0.14	1.97 ± 0.06	0.21
6	5	5	70	19.72 ± 0.54	7.62 ± 0.10	28.19 ± 0.21	5.12 ± 0.09	35.14 ± 0.45	2.21 ± 0.06	2.00 ± 0.10	0.27
7	3	20	70	12.29 ± 0.20	4.55 ± 0.09	16.19 ± 0.25	31.11 ± 0.19	33.52 ± 0.20	1.40 ± 0.04	0.94 ± 0.01	0.18
8	5	20	70	14.23 ± 0.13	5.80 ± 0.04	20.45 ± 0.19	21.32 ± 0.10	34.92 ± 0.31	1.70 ± 0.08	1.59 ± 0.02	0.26
9	3	12.5	40	16.56 ± 0.74	6.40 ± 0.13	22.71 ± 0.79	22.16 ± 0.17	28.33 ± 0.40	1.83 ± 0.06	2.01 ± 0.08	0.21
10	5	12.5	40	20.16 ± 0.67	8.07 ± 0.07	30.86 ± 0.24	13.19 ± 0.17	23.94 ± 0.36	2.21 ± 0.11	1.57 ± 0.05	0.30
11	4	5	40	21.04 ± 0.88	8.28 ± 0.30	34.82 ± 0.57	5.47 ± 0.25	26.46 ± 0.49	2.49 ± 0.06	1.44 ± 0.04	0.25
12	4	20	40	16.35 ± 0.22	6.26 ± 0.18	22.04 ± 0.17	26.68 ± 0.42	25.07 ± 0.18	1.83 ± 0.07	1.78 ± 0.06	0.28
13	4	12.5	10	22.65 ± 0.51	8.66 ± 0.11	40.67 ± 0.56	13.25 ± 0.18	11.37 ± 0.25	2.27 ± 0.04	0.82 ± 0.02	0.18
14	4	12.5	70	16.01 ± 0.31	6.07 ± 0.12	20.89 ± 0.18	16.2 ± 0.08	37.23 ± 0.22	1.73 ± 0.13	1.82 ± 0.02	0.27
15	4	12.5	40	18.09 ± 0.37	7.28 ± 0.09	27.90 ± 0.27	16.61 ± 0.10	26.30 ± 0.29	2.12 ± 0.06	1.82 ± 0.03	0.20
			Min	12.29	4.55	16.19	3.89	10.27	1.40	0.59	0.17
			Max	26.20	9.07	46.04	31.70	40.55	2.59	2.01	0.30

a contour measurer MarSurf XC 20 (Mahr GmbH, Germany) at a feed rate of 0.2 mm/s and a contact force of 0.01 N to measure the radius of the coated Si wafer due to the change of its curvature by residual stresses in the thin film systems after deposition. The hardness and elastic modulus of the thin films were determined by nanoindentation with a Berkovich diamond tip working in continuous stiffness mode, as proposed by Oliver and Pharr [24]. The hardness and elastic modulus were evaluated up to 10 % of the TiSiBCN top layer thickness to avoid influences of the substrate. A Poisson's ratio of 0.25 for TiSiBCN [25] was considered for the calculation of the elastic modulus. Additionally, scratch tests were performed using a Revetest (CSM Instruments SA, Switzerland) equipped with a Rockwell C diamond tip with a radius curvature of 200 µm according to DIN EN ISO 20502:2016-11 [26]. The scratches were evaluated in SEM and EDS and the critical loads L_{c2} and L_{c3} were determined. Tribological tests were carried out using a ball-on-disc tribometer (CSM Instruments, Switzerland). An Al_2O_3 ball was sliding with a load of 2 N against the thin films with a relative velocity of 20 cm/s and 1000 revolutions. The tangential force was measured by an inductive sensor, calculating the coefficient of friction (CoF). The wear coefficients of the thin films were evaluated by measuring the wear volume with a confocal light microscope (Alicona InfiniteFocus, Austria).

3. Results and discussion

In the following, the results and interactions of the deposition parameters on the obtained results are discussed. Finally, a multi-objective optimization was carried out and evaluated. In Table 2 the tribo-mechanical properties of the 15 runs are summarized while the deposition parameters and the exact chemical composition are listed in Table 1.

3.1. Chemical composition and structure of the TiSiBCN thin films

The chemical composition of the TiSiBCN thin films varies with the changes of the deposition parameters according to the CCD plan (see Table 1). As expected with higher C_2H_2 and N_2 gas flow rates the C and N content increases while with greater cathode power at the $TiB_2/TiSi_2$ targets the Ti, Si, and B contents increase in the ranges given in Table 1.

The interaction between the cathode power P_c and the gas flow rates q_{C2H2} and q_{N2} on the chemical composition of the TiSiBCN thin films is shown in Fig. 3. According to the analysis no synergetic interactions between the three factors exist. As the cathode power P_c rises simultaneously the sputtering rate of the $TiB_2/TiSi_2$ targets increases due to a higher ionization and therefore target bombardment through Ar^+ ions [27–29]. As the gas flow rates q_{N2} and q_{C2H2} increase, the Ti and Si contents decrease as observed in previous studies [14]. With higher gas flow rates target poisoning takes place changing the sputtering yield which leads to a decrease in the Ti, B, and Si concentrations [30–32]. The O and Ar contents in TiSiBCN thin films are influenced by the N_2 and C_2H_2 gas flow rates, with the q_{C2H2} and q_{N2} affecting the O level and q_{N2} the Ar content. Lower N and C concentrations reduce O, while higher Ti, Si, and B increase it, likely due to the high reactivity of Ti with O_2 [33,34]. An increased N_2 gas flow rate q_{N2} promotes a higher Ar incorporation within the films.

Fig. 4 shows the XRD patterns of the TiSiBCN thin film systems with the deposition highest B ($Ti_{26}Si_9B_{46}C_4N_{12}$, run 2), highest C ($Ti_{19}Si_7B_{28}C_{32}N_{11}$, run 3), and highest N ($Ti_{18}Si_6B_{22}C_9N_{41}$, run 5) contents. The parameter settings and the chemical composition of the shown films are given in Table 1. The XRD patterns of the TiSiBCN thin film systems are complex due to the multilayered Ti/TiN/TiSiN/TiSiBCN structure, leading to overlays and overlapping of diffraction angles that are difficult to distinguish and assign. For a more precise differentiation, the XRD patterns of the steel substrate and the Ti/TiN/TiSiN interlayer system are analyzed. The diffraction patterns reveal Bragg reflections corresponding to the substrate material, namely α-Fe at 12.9° and Me_6C metal carbides at 10.4°, 11.6°, 12.4°, and 13.5°. The interlayer system Ti/TiN/TiSiN exhibits a Bragg diffraction at 11.1° which can be assigned to (111) β-Ti and (002) α-Ti, while the asymmetric change of the substrate reflection at 11.6° with a broader shoulder towards higher angles is a result of (101) α-Ti. Both Ti reflections stem from the first Ti interlayer. The broad and asymmetric TiN (111), (200), and (202) Bragg reflections are a superposition of the TiN phase of the TiN interlayer and the TiN phase of the TiSiN interlayer. The right shoulders indicate the superposition of the enclosed crystalline TiN phase of the TiSiN interlayer [21].

The reflections of the substrate and the Ti/TiN/TiSiN interlayer system are also detected in the diffraction patterns of the exemplarily chosen TiSiBCN top layers. The main differences for the TiSiBCN thin films are noted from Bragg angles around 10.5° to 11.0° and 17.3° to 18.0° as the intensity and distribution change. Here, different peak shifts are visible at the different runs and therefore originate from the TiSiBCN thin film. The respective reflections may be composed of cubic TiC (10.6°), cubic TiN (10.7°) as well as cubic TiB (10.9°) all with a preferred orientation along the (111) plane. These three phases with a (200) orientation can also be found at 12.3°, 12.4°, and 12.6°, respectively, but the distinction turns out to be difficult due to overlapping with reflections of the interlayer. Furthermore, the broad diffraction angle from 17.3° to 18.0° may also originate from an overlapping of the cubic (202) TiC, TiN, and TiB and shows a similar shift change as the

Table 2
Summary of the results of the CCD plan for the TiSiBCN thin films

Run	Chemical composition	σ_{RS} (GPa)	H (GPa)	E (GPa)	H/E	H^3/E^2	μ (−)	k ($\times10^{-5}$ mm^3/Nm)	L_{c2} (N)	L_{c3} (N)
1	$Ti_{23}Si_9B_{44}C_6N_{14}$	0.26 ± 0.01	34.4 ± 4.5	346.5 ± 28.3	0.099	0.339	0.80 ± 0.05	7.90 ± 0.87	42.1 ± 2.9	68.7 ± 3.9
2	$Ti_{26}Si_9B_{46}C_4N_{12}$	0.53 ± 0.15	39.5 ± 2.7	405.6 ± 17.5	0.097	0.374	[a]0.84 ± 0.03	[a]10.56 ± 0.50	42.0 ± 6.0	66.8 ± 5.8
3	$Ti_{19}Si_7B_{28}C_{32}N_{11}$	0.27 ± 0.12	30.3 ± 1.7	299.1 ± 10.8	0.101	0.311	[b]0.74 ± 0.03	[b]6.36 ± 1.30	30.2 ± 3.0	32.7 ± 4.2
4	$Ti_{22}Si_8B_{37}C_{19}N_{10}$	0.55 ± 0.07	35.6 ± 3.6	344.8 ± 22.4	0.103	0.380	[a]0.84 ± 0.03	[a]10.15 ± 0.75	26.4 ± 6.1	33.6 ± 3.4
5	$Ti_{18}Si_6B_{22}C_9N_{41}$	0.62 ± 0.23	22.6 ± 1.2	233.2 ± 8.0	0.097	0.213	0.85 ± 0.02	8.26 ± 0.39	44.7 ± 1.1	93.7 ± 5.8
6	$Ti_{20}Si_8B_{28}C_5N_{35}$	0.93 ± 0.20	24.9 ± 1.8	248.8 ± 10.8	0.100	0.249	0.74 ± 0.04	7.67 ± 0.04	43.6 ± 9.7	54.1 ± 8.7
7	$Ti_{12}Si_5B_{16}C_{31}N_{34}$	0.49 ± 0.18	20.2 ± 0.8	221.6 ± 6.1	0.091	0.169	[b]0.62 ± 0.06	[b]7.72 ± 0.16	44.3 ± 2.0	69.6 ± 4.0
8	$Ti_{14}Si_6B_{20}C_{21}N_{35}$	0.78 ± 0.15	22.1 ± 0.9	222.3 ± 6.5	0.099	0.217	0.78 ± 0.05	8.59 ± 0.49	35.0 ± 3.8	77.7 ± 2.1
9	$Ti_{17}Si_6B_{23}C_{22}N_{28}$	0.46 ± 0.03	25.8 ± 1.1	252.9 ± 7.5	0.102	0.268	0.68 ± 0.02	8.45 ± 1.21	42.7 ± 5.5	84.00 ± 4.2
10	$Ti_{20}Si_8B_{31}C_{13}N_{24}$	0.65 ± 0.08	29.1 ± 1.1	275.8 ± 6.9	0.106	0.325	0.87 ± 0.02	6.84 ± 1.07	34.5 ± 0.8	–
11	$Ti_{21}Si_8B_{35}C_6N_{27}$	0.62 ± 0.17	29.1 ± 2.9	288.8 ± 18.1	0.101	0.297	[a]0.80 ± 0.10	[a]9.43 ± 2.31	44.6 ± 3.1	79.0 ± 7.4
12	$Ti_{16}Si_6B_{22}C_{27}N_{25}$	0.59 ± 0.18	26.3 ± 1.4	257.7 ± 10.4	0.102	0.273	0.76 ± 0.05	7.34 ± 0.54	44.6 ± 4.7	77.0 ± 5.9
13	$Ti_{23}Si_9B_{41}C_{13}N_{11}$	0.43 ± 0.13	37.2 ± 2.4	353.6 ± 14.9	0.105	0.410	[a]0.83 ± 0.03	[a]12.23 ± 3.82	39.8 ± 5.2	49.3 ± 7.0
14	$Ti_{16}Si_6B_{21}C_{16}N_{37}$	0.59 ± 0.16	23.5 ± 1.5	229.9 ± 9.8	0.102	0.245	0.74 ± 0.01	9.08 ± 0.60	38.6 ± 3.7	–
15	$Ti_{18}Si_7B_{28}C_{17}N_{26}$	0.56 ± 0.12	25.9 ± 1.5	261.3 ± 10.1	0.099	0.254	0.89 ± 0.03	7.53 ± 0.81	41.0 ± 0.5	79.9 ± 8.4
	Min	0.26	20.2	221.6	0.091	0.169	0.62	6.36	26.4	32.7
	Max	0.93	39.5	405.6	0.106	0.410	0.89	12.23	47.3	93.7

[a] Substrate exposed.
[b] TiSiN interlayer exposed.

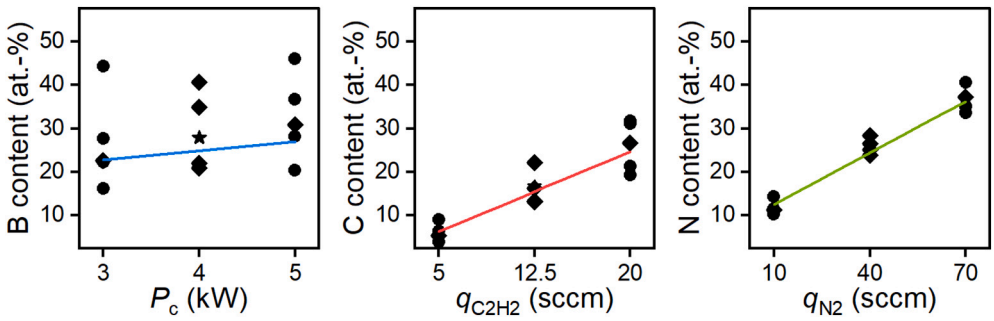

Fig. 3. Influence of cathode power P_c, the C_2H_2 flow rate q_{C2H2}, and N_2 gas flow rate q_{N2} on the B, C, and N contents of the TiSiBCN thin films.

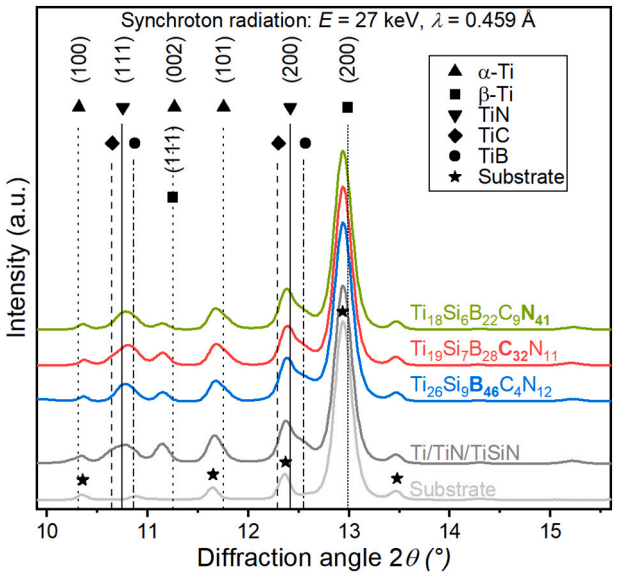

Fig. 4. XRD patterns of the AISI M2 substrate, the Ti/Ti/TiSiN interlayer, and the TiSiBCN thin film systems with the highest B (blue), C (red), and N (green) content. (For interpretation of the references to colour in this figure legend, the reader is referred to the web version of this article.)

(111) diffraction angle. The following discussion will mainly be focused on the (111) diffraction. The $Ti_{26}Si_9B_{46}C_4N_{12}$ (run 2) has the highest B content with (46.0 ± 0.7) at.-%. Both, the (111) and (202) angles exhibit a peak shift towards lower angles due to a superposition of TiB at 10.9° and 17.8°. $Ti_{19}Si_7B_{28}C_{32}N_{11}$ (run 3) shows the highest C content of all runs with (31.7 ± 0.4) at.-%. Here a shoulder formation for (111) TiC can be observed. The (111) TiN reflection is still more pronounced and higher in intensity than TiC while an additional broadening of the (111) and (202) diffractions occurs. In the XRD pattern of $Ti_{18}Si_6B_{22}C_9N_{41}$ (run 5) with the highest N content of (40.6 ± 0.4) at.-% a decrease in (111) TiN intensity can also be observed. The shape of the (111) Bragg diffraction broadens as the intensity of the (111) TiB reflection increases. A change in (002) Ti peak can be observed and can generally be assigned to the TiSiBCN top layers. The addition of N to the Ti lattice leads to the transformation of α-Ti to Ti_2N and finally to TiN. The increase in N is visible in a peak shift of α-Ti to lower angles as N is incorporated in the octahedra sites [31]. The observed alterations in peak positions across $Ti_{26}Si_9B_{46}C_4N_{12}$ (run 2), $Ti_{19}Si_7B_{28}C_{32}N_{11}$ (run 3), and $Ti_{18}Si_6B_{22}C_9N_{41}$ (run 5) stem from varying compositions of B, C, and N, influencing the phase composition of the TiSiBCN thin film. The peak shifts suggest modifications in the crystal lattice structure, potentially attributed to the formation of solid solutions and lattice distortions induced by either the substitution of N and B atoms by C in TiN or TiB, or through the interstitial embedding of atoms within the corresponding lattice. Such lattice distortions are usually characterized by a peak shift towards smaller diffraction angles. Alternatively, the peak shifts may also arise from variations in crystallinity or the increased presence of either TiC, TiN, or TiB within the TiSiBCN thin film which contributes to an increased intensity. Furthermore, in a nanocomposite structure, the embedment in an amorphous phase reduces the crystallite size, thereby resulting in a broadening of the diffractions. Nevertheless, due to the overlays and overlaps in the XRD, the crystallite size could not be determined. The observed peak shifts and changes in the XRD patterns can be attributed to various factors, as supported by previous studies. The investigated TiBCN thin film from Tsai et al. contained also crystalline Ti(C,N) and TiB phases [35]. For instance, the shift of the (111) TiB diffraction angle towards lower angles for $Ti_{26}Si_9B_{46}C_4N_{12}$ (run 2) may be indicative of lattice deformation resulting from the incorporation of N in TiB [20,36]. Additionally, the incorporation of B into TiN has been reported to broaden and diminish the (111) TiN reflection, potentially due to a decrease in crystallite size [37]. Moreover, B may form additional amorphous phases such as a-BN and a-TiB_2, which could inhibit crystalline growth [14,20]. In TiCN thin films, C primarily results in the formation of amorphous phases like a-C and a-CN, although TiC bonds may also increase with increasing C content [38]. However, TiN remains the dominant phase due to its free Gibbs energy at room temperature of −309 kJ/mol compared to TiC with −180 kJ/mol [34]. Consequently, while the TiN reflection is more pronounced and indicative of higher crystallinity, the presence of TiC can be inferred from the shoulder formation at 12.3° [21]. The additional broadening of the (111) and (202) diffractions implicates the incorporation of C in TiN as a solid solution [39]. Additionally, studies on TiBCN nanocomposites have shown that the incorporation of C leads to the formation of a solid solution of Ti(B,C) and Ti(N,C), resulting in a reduction in crystallite size [14]. Furthermore, the peak broadening observed in the XRD patterns could be attributed to crystallite refinement resulting from the increased formation of additional a-C, a-CN phases with high C content, a-BN, a-Si_3N_4 with high N content, and a-TiB_2 with high B content, as reported in previous studies [14,18,20,30]. The XRD diffractions indicate that varying amounts of crystalline Ti(C,N) and TiB phases are embedded within distinct amorphous phases. However, no visible trend for the phase composition depending on the chemical composition can be found.

The SEM micrographs in backscattered electron mode (BSE) of the multilayer structures and the topography of exemplary TiSiBCN thin films with the highest B, C, and N contents are shown in Fig. 5. All TiSiBCN thin films present a cauliflower-like surface morphology. The interlayers Ti, TiN, and TiSiN show a typical columnar-like structure. The TiSiBCN top layers mainly exhibit a dense and glass-like morphology. Thewes et al. noted a comparable glass-like microstructure in SEM image while TEM revealed a finely-grained, isotropic structure on a nanoscale level of PACVD deposited TiSiBCN thin films [19]. The total thicknesses of the thin film systems vary from 1.8 to 2.4 µm and the deposition rate of the TiSiBCN top layer from 0.17 to 0.30 nm/s. A higher cathode power P_c significantly increases the deposition rate by raising the sputtering rate of the targets and the reactivity of the

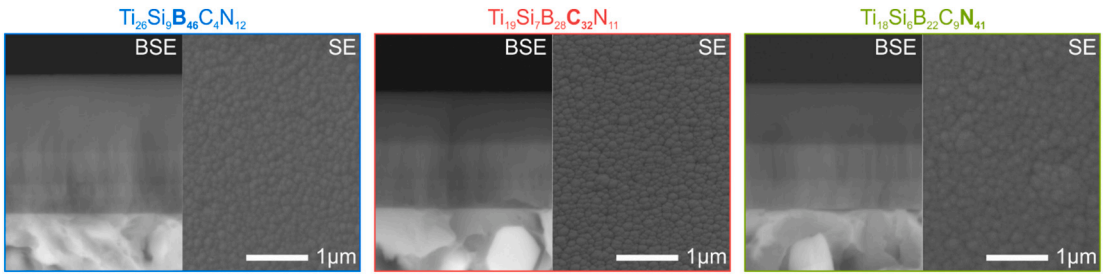

Fig. 5. Exemplary SEM micrographs of the microstructure including and topography of the TiSiBCN thin films with the highest B (blue), C (red), and N (green) content. (For interpretation of the references to colour in this figure legend, the reader is referred to the web version of this article.)

reaction gases. [40–42].

3.2. Mechanical properties of the TiSiBCN thin films

3.2.1. Residual stress

The residual stress σ values of the TiSiBCN thin film systems are listed in Table 2 and Fig. 6 shows the Pareto and effect charts. The influence of the N_2 gas flow rate q_{N2} and the cathode power P_c on the residual stresses within the TiSiBCN thin film systems is statistically significant. Higher q_{N2} and P_c, correspond to increased residual stress σ_{RS}, ranging from 0.62 to 0.89 GPa (see Fig. 6 and Table 2).

A higher cathode power P_c promotes ionization and ion bombardment during thin film growth, as observed in TiSiN and TiCN nanocomposite thin films, where similar correlations were attributed to growth-induced stress by atomic distortion or displacement in the amorphous phase and lattice distortion through substitutional or interstitial solid solution mechanisms [43,44]. While the cathode power P_c prompts the physical distortion of the lattice structure, the N_2 gas flow rate q_{N2} is responsible for the chemical lattice distortion as with different N content the Ti(N) lattice takes different amounts of N atoms [31]. Additionally, the ratio of the crystalline to amorphous phase emerges as a critical factor influencing residual stress in nanocomposites. Previous studies have observed an increase in residual stress with higher crystallinity suggesting a direct correlation between crystalline structures and stress levels [45]. Furthermore, the presence of various phases in TiSiBCN thin films is anticipated to result in mismatches in coefficients of thermal expansion, contributing to thermal-induced stresses [46–48]. Also, as previous studies showed, the incorporation of Ar within the thin films can promote residual stress [21,49]. Despite similar Ar contents around 2 at.-% across different runs (run 5, 6, and 9) of the TiSiBCN thin films no clear correlation can be found here as they vary from 0.46 to 0.96 GPa. So variations in residual stress levels imply additional factors influencing the stress behavior. In amorphous SiBCN thin films, the presence of more flexible Si bonds enables a stress-reduced embedding of Ar atoms, suggesting that the stress effects induced by Ar atoms may be differently absorbed depending on the amorphous phases present [50]. Moreover, the thin film thickness also influences the residual stress, as they increase with a higher thickness while the thickness also increases with higher cathode power P_c. As the increased ion bombardment induces lattice defects the higher thin film thickness leads to a higher defect density promoting residual stress [51].

At last, the stress state of the TiSBCN thin films is influenced by many factors. The residual stress can originate from lattice distortion caused by interstitial and substitutional atoms, physical impact during deposition, and thermal expansion mismatches between the phases. Additionally, the crystalline-to-amorphous phase ratio has an impact on the stress state in nanocomposites. Regarding the significant parameters N_2 gas flow rate q_{N2} and cathode power P_c the main reasons will be chemical and physical lattice distortion.

3.2.2. Hardness and elastic modulus

The DoE analysis identifies both gas flow rates q_{N2} and q_{C2H2} as well as the cathode power P_c as statistically significant parameters influencing the hardness (H) and elastic modulus (E) of TiSiBCN thin films (see Fig. 7). Specifically, the N_2 gas flow rate q_{N2} exhibits the greatest influence on H, while no interactions between the parameters are observed. However, interactions of $q_{N2} \times q_{N2}$, $P_c \times q_{N2}$, and $q_{C2H2} \times q_{N2}$ significantly affect E (see Fig. 7). Both H and E decrease with increasing gas flow rates q_{N2} and q_{C2H2} and N and C content, respectively. In contrast, increasing the cathode power P_c enhances both properties with rising Ti, B, and Si contents. For the TiSiBCN thin films, H ranges from 20.2 to 39.5 GPa and E from 221.6 to 405.6 GPa (see Table 2).

In nanocomposites, the hardness H and toughness result from the Hall-Petch relation including the ratio of the amorphous-to-crystalline phases. The amorphous matrix inhibits crystallite growth and the formation of grain boundaries enhancing hardness H by preventing dislocation movements to a certain degree (inverse Hall-Petch effect) [52]. Si will more likely form an amorphous phase like a-Si_3N_4 because of the low free Gibbs energy of −647.3 kJ/mol contributing to a nanocomposite structure [34]. According to Patscheider et al., a Si content in TiSiN thin films above 10 at.-% decreases H and E due to the increased volume fraction of a-Si_3N_4 [11]. Given that the TiSiBCN thin films here have only a maximum Si content of 9 at.-%, the formation of other N-based amorphous phases besides a-Si_3N_4 like a-BN and a-CN could participate in the growth of the amorphous phase ratio as the N_2 gas flow rate q_{N2} and the N content increases [14,17]. Moreover, the increase of

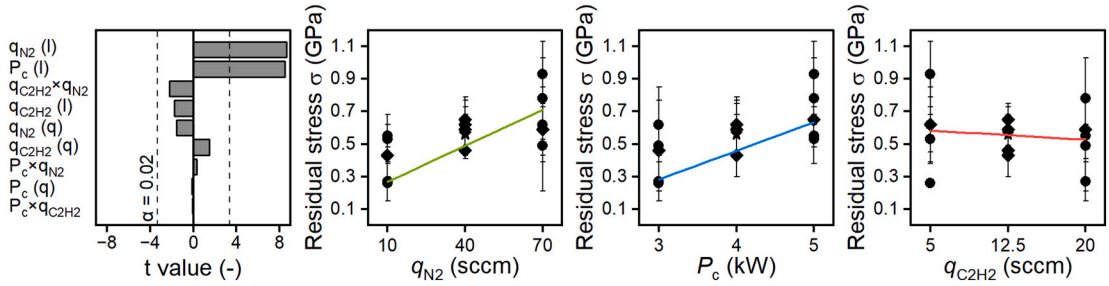

Fig. 6. Statistical significance and influence of the N_2 gas flow rate q_{N2}, the C_2H_2 gas flow rate q_{C2H2}, and cathode power P_c on the residual stress σ_{RS} of the TiSiBCN thin films.

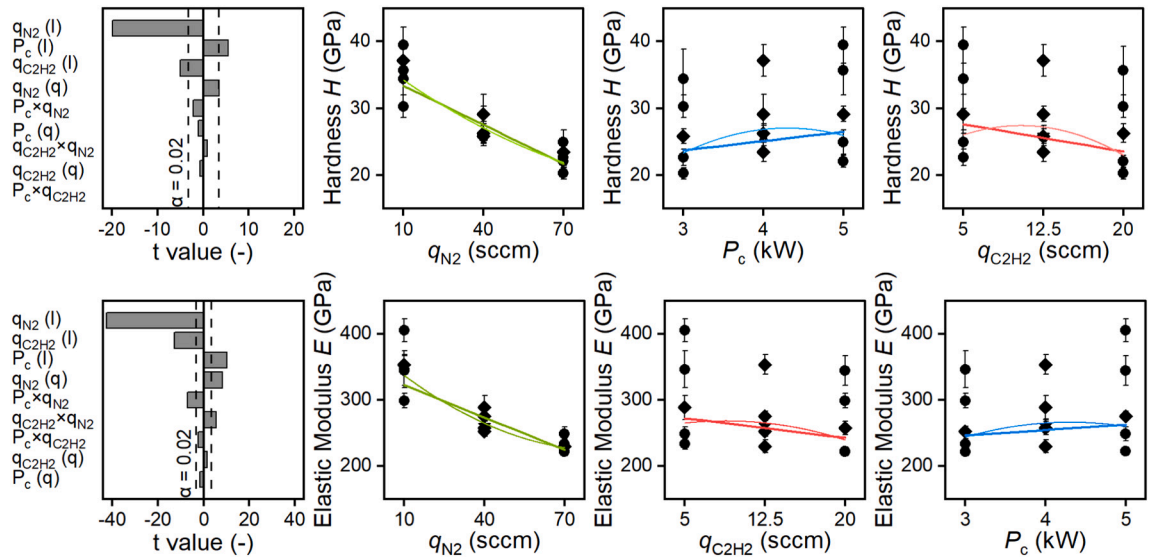

Fig. 7. Statistical significance and influence of N_2 gas flow rate q_{N2}, the C_2H_2 gas flow rate q_{C2H2}, and the cathode power P_c on the hardness H (above) and elastic modulus E (below) of the TiSBCN thin films.

the C_2H_2 gas flow rate q_{C2H2}, and consequently the higher C content promotes the formation of additional soft amorphous C-based phases, which in return reduces the hardness H and elastic modulus E [44]. However, higher Ti and B contents increase both mechanical properties, favoring the formation of a nanocomposite with more hard crystalline phases. Accordingly, Ti and B participate in the formation of crystalline phases Ti(C,N) and TiB as observed in the XRD patterns above. The highest hardness was reached for $Ti_{26}Si_9B_{46}C_4N_{12}$ (run 2) with the highest B and Ti content of (46.0 ± 0.7) at.-% and (26.2 ± 0.8) at.-% with low C and N contents. Here a higher amount of hard crystalline Ti(C,N) and TiB phases is expected to enhance H as shown in TiBN thin films where coexisting crystalline Ti—N and Ti—B enhance both hardness and high toughness [36], with the formation of TiCN solid solution also contributing to H enhancement [7]. The $Ti_{12}Si_5B_{16}C_{31}N_{34}$ (run 7) with the lowest H of (20.2 ± 0.8) GPa contains a relatively high amount of C and N while the Ti and B contents are at the lowest. Indicating that more amorphous C- and N-based phases are formed lowering H and E of the nanocomposite. Consequently, the ratio of amorphous phase forming elements (C, N, and Si) to crystallite forming elements (Ti and B) *(Si + C + N)/(Ti + B)* shows a correlation regarding H and E, with the highest hardness at a ratio of 0.3 (see Fig. 8). However, it must be taken into account that the crystallite size also has a significant effect on H and E, as described by the Hall-Petch relationship and the associated hardness enhancement.

To obtain information about the toughness and resistance to plastic deformation of the TiSiBCN thin films the H/E and H^3/E^2 ratios are calculated (see Table 2). The deposition parameters considered do not show a statistically significant effect concerning the H/E and H^3/E^2 ratios. Considering *(Si + C + N)/(Ti + B)*, for H/E a maximum occurs at a ratio of ≈1 for the estimated trend line (see Fig. 8). Here a favorable ratio of amorphous and crystalline phases is expected. H^3/E^2 increases with lower *(Si + C + N)/(Ti + B)* due to a decrease in hard crystalline phases (see Fig. 8).

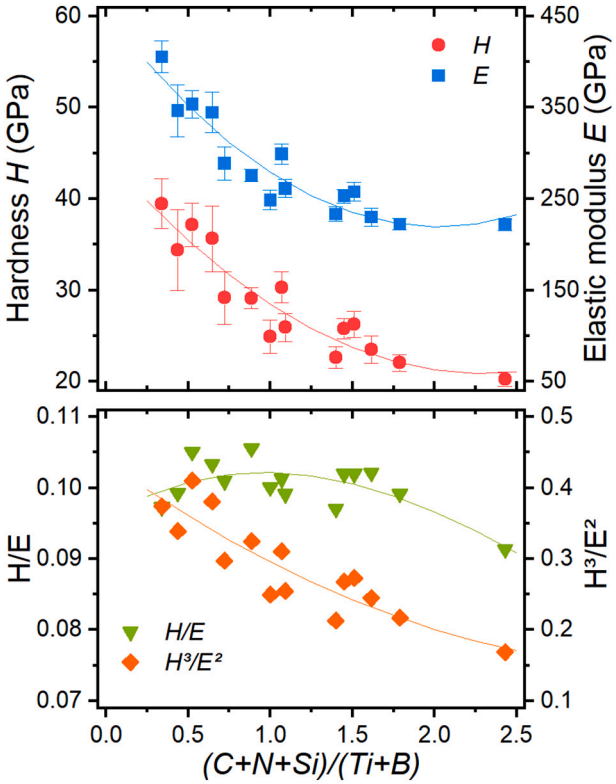

Fig. 8. Hardness H, elastic modulus E, H/E, and H^3/E^2 in relation to the *(Si + C + N)/(Ti + B)* ratio of the TiSiBCN thin films

3.3. Adhesion behavior of the TiSiBCN thin films

The adhesion behavior of the TiSiBCN thin films was determined with scratch test. The critical loads L_{c2} and L_{c3} that result from the scratch test describe the adhesive failures of the thin film systems and are exemplary shown in Fig. 9. At L_{c2} adhesive failure by chipping of the thin film at the edge of the scratch track appears. Total failure of the thin film by complete exposure of the substrate occurs at L_{c3}. All results can be found in Table 2. Apart from run 3, 4, 6, and 13 (see Fig. 9) all other thin film systems have L_{c3} values of >60 N, which according to Ma et al. represent the lower limit for industrial application [53]. The thin film systems in run 10 and 14 remained intact and only showed chipping at the edge of the scratch track.

$Ti_{18}Si_7B_{28}C_{17}N_{26}$ (run 15) has the best critical load L_{c2} = 47.3 N with moderate C and N contents. The highest value for L_{c3} showed $Ti_{20}Si_8B_{31}C_{13}N_{24}$ (run 10) and $Ti_{16}Si_6B_{21}C_{16}N_{37}$ (run 14) where any delamination occurred. Both thin films have a moderate C concentration

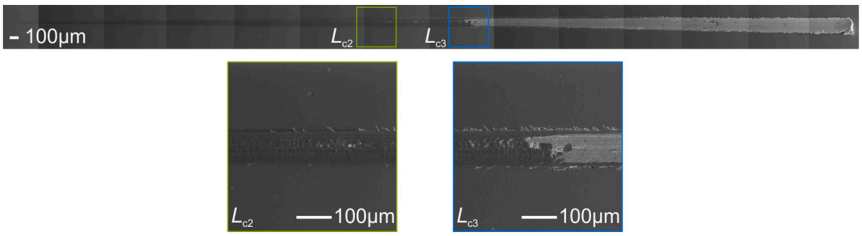

Fig. 9. SEM micrographs of L_{c2} and L_{c3} of an exemplary scratch of $Ti_{23}Si_9B_{41}C_{13}N_{11}$ (run 13) thin film.

while Ti, B, and N are relatively high. The lowest L_{c3} value is measured for $Ti_{19}Si_7B_{28}C_{32}N_{11}$ (run 3) with $L_{c3} = 32.7$ N containing a low N and the highest C content. L_{c2} is statistically affected by the interaction of the gas flow rates q_{N2} and q_{C2H2}, and L_{c3} by the N_2 gas flow rate q_{N2} (see Fig. 10). At the lowest C_2H_2 gas flow rate $q_{C2H2} = 5$ sccm and increasing of N_2 gas flow rate q_{N2} the critical load L_{c2} decreases. At the highest level of C_2H_2 gas flow rate $q_{C2H2} = 10$ sccm an increase of the critical load L_{c2} takes place. The critical load L_{c2} can be affected by the *H-E* ratios, microstructure, and thin film thickness [54,55]. But no evident correlation can be found here. With lower C and high N content mainly hard crystalline TiN phases emerge (see Fig. 4) which can benefit a lower toughness and lead to a brittle film. With high C concentrations, a more ductile nanocomposite is expected due to additional assumed a-C phases leading to an increased critical load L_{c2}.

The effect diagrams reveal a higher adhesion strength L_{c3} with a higher N_2 gas flow rate q_{N2} and therefore higher N concentration. At the same time, there is a decrease in hardness H (see Fig. 7). During the scratch test, increased compressive stresses occur in front of the diamond tip within the coating accumulating the energy before the threshold for elastic deformation is reached. Thin film systems with lower hardness show a tendency to absorb this energy in the form of elastic deformation over a longer distance during the scratch test [56,57].

Overall, the adhesion behavior depends on many other factors that result from roughness, toughness, and residual stress within the thin film and between the different layers and the substrate [21,58–60]. While these properties in turn influence each other. However, no correlation was found depending on further thin film properties. Focusing on the gas flow rates declared as the significant factors, it can be concluded that a certain toughness is necessary to achieve a high adhesion strength. The gas flow rates promote the formation of hard Ti(C,N) phases and the excess N and C atoms form more likely soft a-phases that enhance toughness and can absorb deformation forces up to a certain degree.

3.4. Tribological properties

The results of the tribological test against Al_2O_3 of the TiSiBCN thin films can be found in Table 2. It should be noted that the thin film systems from $Ti_{26}Si_9B_{46}C_4N_{12}$ (run 2), $Ti_{22}Si_8B_{37}C_{19}N_{10}$ (run 4), $Ti_{21}Si_8B_{35}C_6N_{27}$ (run 11), and $Ti_{23}Si_9B_{41}C_{13}N_{11}$ (run 13) experienced tribological failure, leading to substrate exposure. In $Ti_{19}Si_7B_{28}C_{32}N_{11}$ (runs 3) and $Ti_{12}Si_5B_{16}C_{31}N_{34}$ (run 7), the TiSiBCN top layers were removed to the TiSiN interlayer. Consequently, a systematic statistical analysis of the tribological parameters such as coefficient of friction (CoF) μ and wear rate k cannot be carried out. Nevertheless, the calculated effect diagrams suggest that higher cathode power P_c leads to increased CoF μ and wear rates k, while higher gas flow rates q_{C2H2} and q_{N2} result in decreased CoF μ and wear rates k, indicating a potential trend (see Fig. 11). The intact thin films show CoF μ in a range from 0.68 to 0.89 and k from 6.84 to 9.08 $\times$ 10^{-5} mm^3/Nm (see Table 2).

The wear tracks of TiSiBCN thin films with the highest B, C, and N content including EDS images indicating O and Fe are shown in Fig. 12. $Ti_{26}Si_9B_{46}C_4N_{12}$ (run 2) with the highest B content does not withstand the tribological load, and the substrate is exposed. For $Ti_{19}Si_7B_{28}C_{32}N_{11}$ (runs 3) with the highest C content the interlayer is visible which is illustrated by the increased N content in the middle of the wear track and a higher presence of O indicates the formation of oxide layers and particles. The wear track of $Ti_{18}Si_6B_{22}C_9N_{41}$ (run 5) exhibits smoother surfaces due to the flattening of roughness asperities, along with the presence of scale-like oxide adhesions. These local material adhesions along the sliding direction result from the adhesive wear of the thin film system as a result of shear and abrasion of the thin films against the

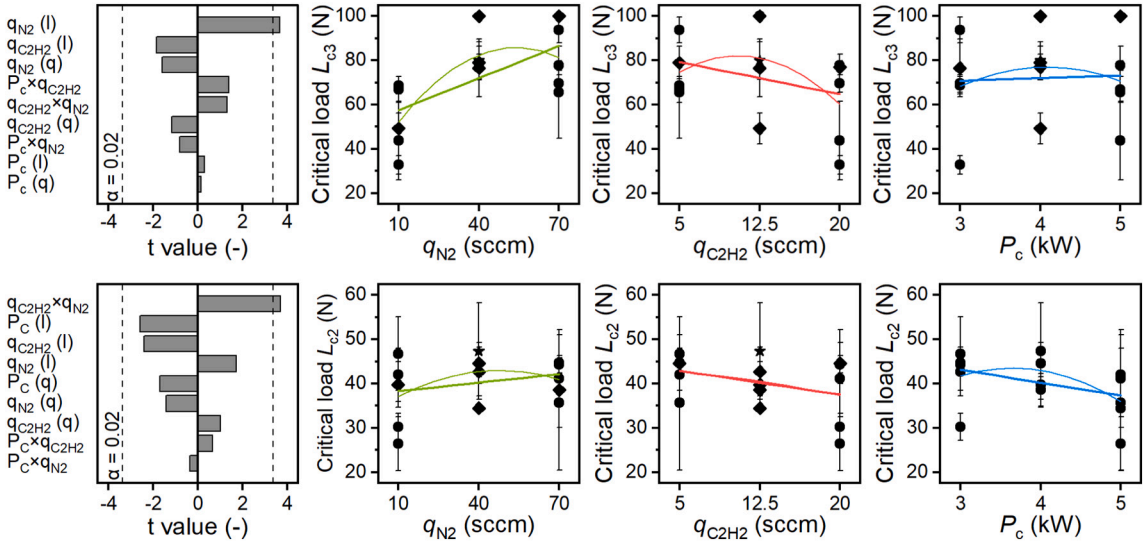

Fig. 10. Statistical significance and influence of the cathode power P_c, the C_2H_2 gas flow rate q_{C2H2}, and the N_2 gas flow rate q_{N2} on the critical loads L_{c2} and L_{c3} determined by scratch test of the TiSiBCN thin films.

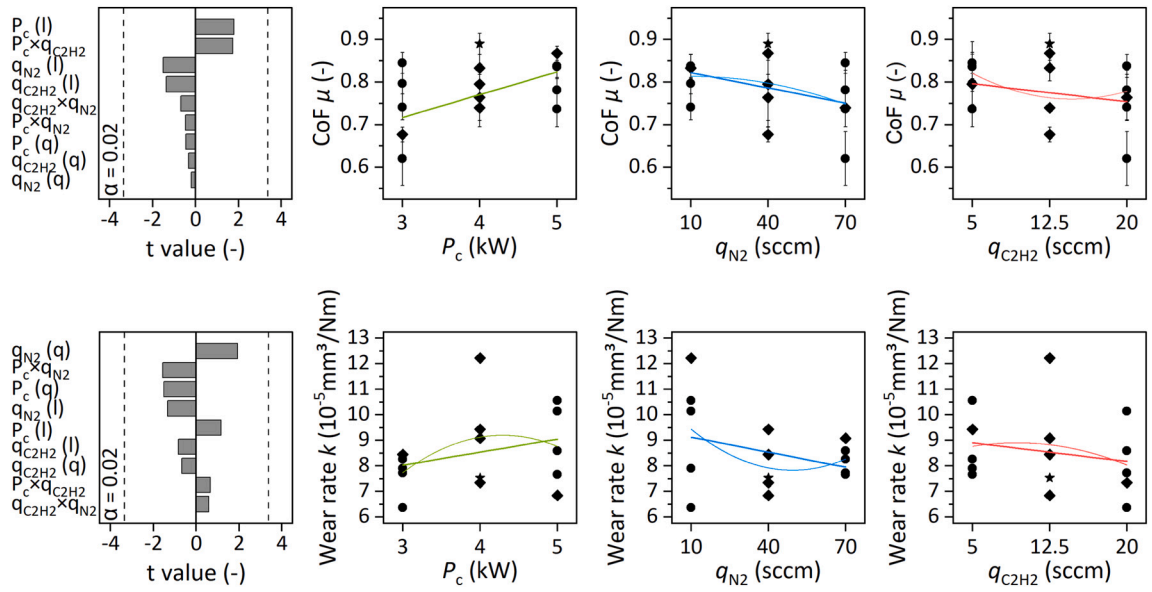

Fig. 11. Statistical significance and influence of the N_2 gas flow rate q_{N2}, the C_2H_2 gas flow rate q_{C2H2}, and the cathode power P_c on the CoF μ and the wear rate k of the TiSiBCN thin films.

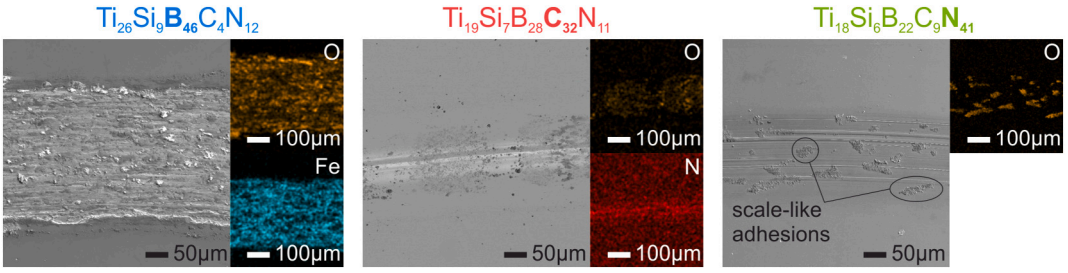

Fig. 12. SEM micrographs of wear tracks with EDS analysis of O, N, and Fe of the TiSiBCN thin film systems with the highest B (blue), C (red), and N (green) content. (For interpretation of the references to colour in this figure legend, the reader is referred to the web version of this article.)

Al_2O_3 ball [61]. As the oxide scales are visibly sheared it is believed that they are formed from easily agglomerating softer amorphous oxide phases. No Al from the Al_2O_3 counter body is detected in the wear track. Overall, the wear of the Al_2O_3 ball was low (0.01–1.03 × 10^{-5} mm^3/Nm) or could not be measured. Besides adhesion mechanisms and tribo-oxidation between the ball and the TiSiBCN surface abrasion occurs due to the formation of small hard oxide particles, leaving grooves in the sliding direction within the wear track and wearing off the top layer (see Fig. 12).

What is noticeable is that the thin films that failed contain a relatively high B content and low N content with high hardness. Lin et al. described that TiBCN films with low N content tend to be brittle due to the presence of hard crystalline TiB_2, which favors higher CoF and wear rates [14]. Increased C and N contents and the formation of their amorphous phases benefit low friction [14,17,18]. Opposing the friction coefficient μ of the intact thin film with the ratio $(Si + C + N)/(Ti + B)$ reveals a trend. Higher ratios correspond to lower CoF (see Fig. 13 left). Especially a-CN and a-C have self-lubricating characteristics, that diminish friction when the proportion is sufficient. Ma et al. proposed a high C content of over 30 at.-% to reduce the friction of TiSiCN thin films

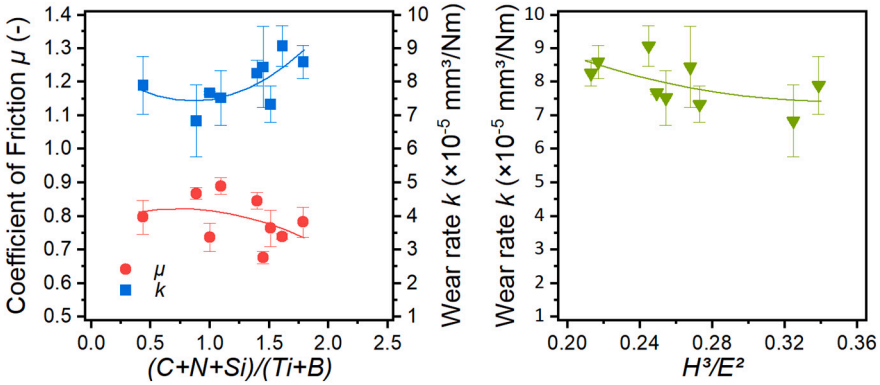

Fig. 13. Coefficient of friction μ and wear rate k in relation to the $(Si + C + N)/(Ti + B)$ ratio of the intact TiSiBCN thin films.

by forming graphite-like lubricious films [62]. The TiSiBCN thin films with the highest C content exceeding 30 at.-% are $Ti_{19}Si_7B_{28}C_{32}N_{11}$ (runs 3) and $Ti_{12}Si_5B_{16}C_{31}N_{34}$ (run 7). The decreasing trend of the CoF μ with increasing C_2H_2 gas flow rate q_{C2H2} and therefore C content becomes apparent. Nevertheless, the top layer of $Ti_{12}Si_5B_{16}C_{31}N_{34}$ (run 7) was removed, likely due to its lowest H (20.2 ± 0.8) GPa and H-E ratios, along with the highest $(Si + C + N)/(Ti + B)$ attributed to an additional high N content of 33.5 at.-%. $Ti_{19}Si_7B_{28}C_{32}N_{11}$ (runs 3) reaches a moderate CoF of 0.74 despite a C content >30 at.-%.

Putting the wear rate k into relation with $(Si + C + N)/(Ti + B)$ an increasing and with H^3/E^2 a decreasing trend is observed (see Fig. 13). Reduction in wear for TiSiCN thin films has been linked to enhanced mechanical properties and resistance against plastic deformation [63]. For TiBCN thin films the increase in the N content promoted wear due to a decrease in hard crystal phases [14]. Lu et al. explained that the wear behavior is mainly influenced by the phase composition rather than hardness [61]. This notion can be supported by the current findings as the proportion $(Si + C + N)/(Ti + B)$ influences the mechanical properties (see Fig. 13 and Fig. 8). Briefly, higher gas flow rates q_{N2} and q_{C2H2} tend to reduce friction due to the formation of lubricating amorphous phases, but this is accompanied by a decrease in hardness, resulting in lower wear resistance.

3.5. Optimization of the TiSiBCN thin films

After the analysis of correlations of the deposition parameters the N_2 gas flow rate q_{N2}, the C_2H_2 gas flow rate q_{C2H2}, and the cathode power P_c on the tribo-mechanical properties and chemical composition the optimization process was conducted. Disregarding the lack of statistical significance in some tribo-mechanical properties. Therefore hardness H, the elastic modulus E, and the adhesion behavior L_{c3} have to be maximized, whereas the CoF μ and the wear rate k have to be minimized concerning the use of TiSiBCN thin films for tool applications The calculated values for the deposition parameters cathode power P_c, C_2H_2 gas flow rate q_{C2H2}, and N_2 gas flow rate q_{N2}, as well as the estimated properties for the highest desirability possible, are given in Table 3. Due to the consideration of the properties adhesion behavior L_{c3}, the friction coefficient μ, and the wear rate k which are not significantly affected by the deposition parameters the calculated desirability reached only a value of 0.58.

The chemical and mechanical properties hardness H, elastic modulus E, and adhesion strength L_{c3} reached a high accuracy of 94 to 101 %, whereas the deviation of the tribological values CoF μ and wear rate k with 15 % and 74 % is relatively high. Also, the correlation of the focused tribo-mechanical properties with the chemical ratio $(C + N + Si)/(Ti + B)$ exhibits similar results. For the hardness H, the elastic modulus E, and the H-E ratios the predicted values match the calculated curve quite well but for the tribological trend lines the tribological properties show a greater deviation (see Fig. 14). This is due to the high spread of the measured values in general and the resulting lack of statistical significance which makes it less precise to predict the tribological behavior. Therefore, despite the deviation of the tribological properties the optimization of the DoE as well as the chemical ratio $(Si + C + N)/(Ti + B)$ shows precise results and can be used as an effective tool to estimate the hardness H and elastic modulus E of TiSiBCN thin films.

4. Conclusion

The Design of Experiments analysis of TiSiBCN thin films revealed the complexity of multi-element nanocomposites. The variation of the deposition parameters N_2 gas flow rate q_{N2}, cathode power of the TiB_2/$TiSi_2$ targets P_c, and the C_2H_2 flow rate q_{C2H2} affects the chemical, structural, and tribo-mechanical properties to different degrees or are indirectly influenced by other properties. The chemical composition is strongly linked to the respective deposition parameters. The higher the gas flow rates q_{N2} and q_{C2H2} the more N and C are in the TiSiBCN thin films and the higher P_c the higher the Ti, B, and Si content. The chemical composition further affects the crystalline phase formation. Due to the multi-layered structure, the XRD analysis turned out to be difficult. Nevertheless, the formation of crystalline Ti(N,C) and TiB could be demonstrated through peak shifts and asymmetries depending on the chemistry but with no evident trend regarding the deposition parameters. The lack of crystalline Si-based phases indicates their existence in amorphous form. In connection with the visible glass-like structure of the TiSiBCN thin films, the formation of a nanocomposite is expected. The tribo-mechanical properties are mainly influenced by the phases which are directly coupled to the chemical composition. For this purpose, the chemical ratio $(C + N + Si)/(Ti + B)$ was additionally established to estimate a correlation regarding the chemical composition on the tirbo-mechanical properties. The residual stress in TiSiBCN thin films increases with a higher cathode power P_c and N_2 gas flow rate q_{N2}. Additionally, the incorporation of Ar and thin film thickness can contribute to variations in residual stress levels but with no evident correlation here. The hardness H and elastic modulus E exhibited significant dependence on all deposition parameters but mainly on the N_2 gas flow rate q_{N2}. Generally, higher gas flow rates q_{N2} and q_{C2H2} reduce H and E, and increasing the cathode power P_c enhances them. As there was no correlation found with the residual stress the main cause analyzed here was the chemical composition ratio $(C + N + Si)/(Ti + B)$. A reasonable correlation was found that with higher $(C + N + Si)/(Ti + B)$ and an expected higher amorphous phase ratio the thin films softened. Also for H/E and H^3/E^2 trends were observed by reducing the toughness H/E with higher $(C + N + Si)/(Ti + B)$ and reaching a maximum for H^3/E^2 and therefore the resistance against plastic deformation around $(C + N + Si)/(Ti + B) \approx 1$. The adhesion behavior determined by the critical loads L_{c2} and L_{c3} is statistically influenced by the reaction gas flow rates q_{N2} and q_{C2H2}. A higher stress absorption ability due to a favorable toughness which depends on the phase structure seems to favor a better adhesion behavior. Since the tribological properties friction coefficient μ and wear rate k result from a complex interplay, no clear dependency was noted. But a trend to the chemical ratio $(C + N + Si)/(Ti + B)$ is apparent. In terms of H^3/E^2 to $(C + N + Si)/(Ti + B)$, the TiSiBCN thin films with a chemical ratio of 1 tend to show the least wear but also increased friction. With a higher chemical ratio $(C + N + Si)/(Ti + B)$ the nanocomposites get softer, and therefore the wear resistance diminishes but decreases friction. The DoE is a promising approach to adjust and predict, especially the chemical and mechanical properties of TiSiBCN. But also the chemical ratio $(C + N + Si)/(Ti + B)$ offers a simplified prediction.

Overall, the diverse behaviors observed in the TiSiBCN nanocomposites are the result of intricate interactions between deposition parameters, chemical and tribo-mechanical properties. Understanding

Table 3
Multi-objective optimization of the tribo-mechanical properties, estimation of the DoE parameters, and comparison to the as-proposed deposited TiSiBCN thin film

	P_c	q_{C2H2}	q_{N2}	Ti	Si	B	C	N	(C + N + Si)/(Ti + B)	H	E	L_{c3}	μ	k
	(kW)	(sccm)	(sccm)	(at.-%)					(−)	(GPa)	(GPa)	(N)	(−)	($\times 10^{-5}$ mm^3/Nm)
Optimization										Max.	Max.	Max.	Min.	Min.
Prediction	3	14.8	37.2	16.5	6.4	22.9	25.1	25.4	1.45	25.2	249	78.6	0.73	6.6
Reality	3	14.8	37.2	16.3	6.1	21.4	26.0	26.4	1.56	25.0	252	87.2	0.79	9.7
Accuracy				99 %	95 %	93 %	104 %	104 %	108 %	99 %	101 %	94 %	115 %	174 %

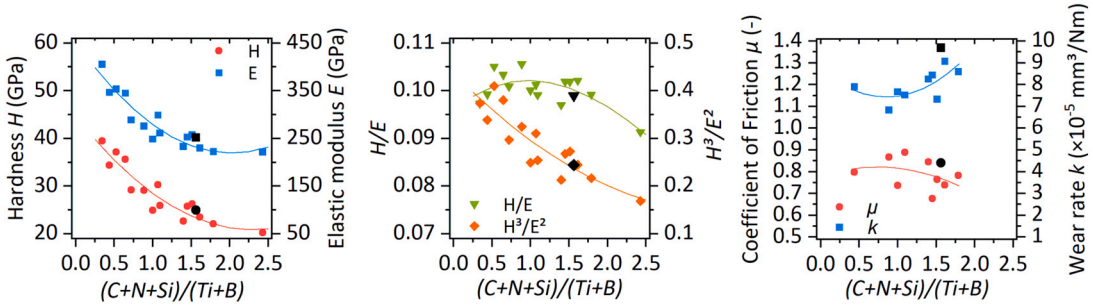

Fig. 14. Chemical ratio *(Si + C + N)/(Ti + B)* compared to the hardness *H*, elastic modulus *E*, CoF μ, and wear rate *k* of the deposited TiSiBCN thin film (black points) of DoE prediction.

these relationships is crucial for optimizing the deposition process and tailoring thin film properties to specific applications and the DoE is a useful tool to adjust complex nanocomposites like TiSiBCN.

CRediT authorship contribution statement

Wolfgang Tillmann: Writing – review & editing, Supervision, Resources. **Julia Urbanczyk:** Writing – original draft, Visualization, Project administration, Investigation, Conceptualization. **Ahmad Zahid Ebady:** Writing – review & editing, Visualization, Investigation. **Alexander Thewes:** Writing – review & editing. **Günter Bräuer:** Writing – review & editing. **Nelson Filipe Lopes Dias:** Writing – review & editing, Supervision.

Declaration of Generative AI and AI-assisted technologies in the writing process

During the preparation of this work the authors used ChatGPT (https://chat.openai.com/) in order to improve the readability of the paper. After using this tool, the authors reviewed and edited the content as needed and take full responsibility for the content of the publication.

Declaration of competing interest

The authors declare that they have no known competing financial interests or personal relationships that could have appeared to influence the work reported in this paper.

Acknowledgments

This work was supported by the German Research Association (DFG) within the project TI 343/180-1. The authors gratefully acknowledge the Institute of Machining Technology (ISF), Dortmund for providing contour measurements and DELTA for providing synchrotron radiation and for the technical support at beamline BL9 during the X-ray diffraction experiments.

Data availability

Data will be made available on request.

References

[1] E.O. Ezugwu, C.I. Okeke, Tool life and wear mechanisms of TiN coated tools in an intermittent cutting operation, J. Mater. Process. Technol. 116 (2001) 10–15, https://doi.org/10.1016/S0924-0136(01)00852-4.
[2] E.J.A. Armarego, S. Verezub, P. Samaranayake, The effect of coatings on the cutting process, friction, forces and predictive cutting models in machining operations, Proc. Inst. Mech. Eng. B J. Eng. Manuf. 216 (2002) 347–356, https://doi.org/10.1243/0954405021520012.
[3] F. Klocke, Grundlagen, in: F. Klocke (Ed.), Fertigungsverfahren 4, Springer Berlin Heidelberg, Berlin, Heidelberg, 2017, pp. 5–200.
[4] P.C. Siow, J.A. Ghani, M.J. Ghazali, T.R. Jaafar, M.A. Selamat, C.H. Che Haron, Characterization of TiCN and TiCN/ZrN coatings for cutting tool application, Ceram. Int. 39 (2013) 1293–1298, https://doi.org/10.1016/j.ceramint.2012.07.061.
[5] M. Berger, S. Hogmark, Evaluation of TiB2 coatings in sliding contact against aluminium, Surf. Coat. Technol. 149 (2002) 14–20, https://doi.org/10.1016/S0257-8972(01)01361-5.
[6] M. Folea, A. Roman, N.-B. Lupulescu, An overview of DLC coatings on cutting tools performance, Academic Journal of Manufacturing Engineering 8 (2010) 30–36.
[7] N. Donnelly, M. McConnell, D.P. Dowling, J.D. O'Mahony, A comparison between the tribological and mechanical properties of TiN and TiCN, MSF 325-326 (2000) 141–148, https://doi.org/10.4028/www.scientific.net/MSF.325-326.141.
[8] T. Polcar, T. Kubart, R. Novák, L. Kopecký, P. Široký, Comparison of tribological behaviour of TiN, TiCN and CrN at elevated temperatures, Surf. Coat. Technol. 193 (2005) 192–199, https://doi.org/10.1016/j.surfcoat.2004.07.098.
[9] N. Madaoui, N. Saoula, B. Zaid, D. Saidi, A.S. Ahmed, Structural, mechanical and electrochemical comparison of TiN and TiCN coatings on XC48 steel substrates in NaCl 3.5% water solution, Appl. Surf. Sci. 312 (2014) 134–138, https://doi.org/10.1016/j.apsusc.2014.04.167.
[10] L. Qiu, Y. Du, S. Wang, K. Li, L. Yin, L. Wu, Z. Zhong, L. Albir, Mechanical properties and oxidation resistance of chemically vapor deposited TiSiN nanocomposite coating with thermodynamically designed compositions, Int. J. Refract. Met. Hard Mater. 80 (2019) 30–39, https://doi.org/10.1016/j.ijrmhm.2018.12.018.
[11] J. Patscheider, T. Zehnder, M. Diserens, Structure–performance relations in nanocomposite coatings, Surf. Coat. Technol. 146-147 (2001) 201–208, https://doi.org/10.1016/S0257-8972(01)01389-5.
[12] J.B. Choi, K. Cho, M.-H. Lee, K.H. Kim, Effects of Si content and free Si on oxidation behavior of Ti–Si–N coating layers, Thin Solid Films 447-448 (2004) 365–370, https://doi.org/10.1016/S0040-6090(03)01083-6.
[13] Y.H. Lu, Y.G. Shen, K.Y. Li, H. Chen, Effects of nitrogen content on nanostructure evolution, mechanical behaviors and thermal stability in Ti–B–N thin films, Surf. Coat. Technol. 201 (2006) 1228–1235, https://doi.org/10.1016/j.surfcoat.2006.01.045.
[14] J. Lin, J.J. Moore, B. Mishra, M. Pinkas, W.D. Sproul, The structure and mechanical and tribological properties of TiBCN nanocomposite coatings, Acta Mater. 58 (2010) 1554–1564, https://doi.org/10.1016/j.actamat.2009.10.063.
[15] W. Tillmann, G. Bejarano, F. Hoffmann, Deposition of hard and adherent TiBCN films for cutting tools applications, Phys. Status Solidi A 209 (2012) 1520–1525, https://doi.org/10.1002/pssa.201228130.
[16] Q.H. Luo, Y.H. Lu, Microstructure and mechanical properties of reactive magnetron sputtered Ti–B–C–N nanocomposite coatings, Appl. Surf. Sci. 258 (2011) 1021–1026, https://doi.org/10.1016/j.apsusc.2011.08.053.
[17] X. Chen, Z. Wang, S. Ma, V. Ji, Microstructure, mechanical and tribological properties of Ti–B–C–N films prepared by reactive magnetron sputtering, Diam. Relat. Mater. 19 (2010) 1336–1340, https://doi.org/10.1016/j.diamond.2010.07.002.
[18] K.H. Kim, J.T. Ok, S. Abraham, Y.-R. Cho, I.-W. Park, J.J. Moore, Syntheses and mechanical properties of Ti–B–C–N coatings by a plasma-enhanced chemical vapor deposition, Surf. Coat. Technol. 201 (2006) 4185–4189, https://doi.org/10.1016/j.surfcoat.2006.08.051.
[19] A. Thewes, L. Bröcker, E.T.K. George, G. Bräuer, M. Paulus, C. Sternemann, H. Paschke, T. Brückner, S. Lechner, S. Müller, Ti-Si-B-C-N plasma enhanced chemical vapor deposition nanocomposite coatings for high temperature applications, Thin Solid Films 760 (2022) 139507, https://doi.org/10.1016/j.tsf.2022.139507.
[20] I.W. Park, B. Mishra, K.H. Kim, J.J. Moore, Multifunctional Ti-Si-B-C-N Tribological nanocomposite coatings for aerospace applications, MSF 539-543 (2007) 173–180, https://doi.org/10.4028/www.scientific.net/MSF.539-543.173.
[21] W. Tillmann, J. Urbanczyk, A. Thewes, G. Bräuer, N.F. Lopes Dias, Effect of the TiSiN interlayer properties on the adhesion and mechanical properties of multilayered TiSiCN thin films, Surf. Coat. Technol. 478 (2024) 130467, https://doi.org/10.1016/j.surfcoat.2024.130467.
[22] C. Krywka, C. Sternemann, M. Paulus, N. Javid, R. Winter, A. Al-Sawalmih, S. Yi, D. Raabe, M. Tolan, The small-angle and wide-angle X-ray scattering set-up at

beamline BL9 of DELTA, Erratum, J. Synchrotron. Rad. 14 (2007) 391, https://doi.org/10.1107/S0909049507020729.
[23] G. Janssen, M.M. Abdalla, F. van Keulen, B.R. Pujada, B. van Venrooy, Celebrating the 100th anniversary of the Stoney equation for film stress: developments from polycrystalline steel strips to single crystal silicon wafers, Thin Solid Films 517 (2009) 1858–1867, https://doi.org/10.1016/j.tsf.2008.07.014.
[24] W.C. Oliver, G.M. Pharr, An improved technique for determining hardness and elastic modulus using load and displacement sensing indentation experiments, J. Mater. Res. 7 (1992) 1564–1583, https://doi.org/10.1557/JMR.1992.1564.
[25] I.W. Park, B. Mishra, K.H. Kim, J.J. Moore, Multifunctional Ti-Si-B-C-N tribological nanocomposite coatings for aerospace applications, MSF 539-543 (2007) 173–180, https://doi.org/10.4028/www.scientific.net/MSF.539-543.173.
[26] DIN EN ISO 20502:2016-11, Hochleistungskeramik_- Bestimmung der Haftung von keramischen Schichten mit dem Ritztest (ISO_20502:2005 einschließlich Cor_1: 2009); Deutsche Fassung EN_ISO_20502:2016, Beuth Verlag GmbH, Berlin.
[27] T. Nakano, N. Hirukawa, S. Saeki, S. Baba, Effects of target voltage during pulse-off period in pulsed magnetron sputtering on afterglow plasma and deposited film structure, Vacuum 87 (2013) 109–113, https://doi.org/10.1016/j.vacuum.2012.03.010.
[28] T. Nguyen, S. Ulrich, J. Bsul, S. Beauvais, W. Burger, A. Albers, M. Stüber, J. Ye, Influence of argon gas pressure and target power on magnetron plasma parameters, Diam. Relat. Mater. 18 (2009) 995–998, https://doi.org/10.1016/j.diamond.2009.01.015.
[29] W. Tillmann, D. Stangier, P. Schröder, Investigation and optimization of the tribo-mechanical properties of CrAlCN coatings using design of experiments, Surf. Coat. Technol. 308 (2016) 147–157, https://doi.org/10.1016/j.surfcoat.2016.07.110.
[30] P. Mahato, R.J. Singh, L.C. Pathak, S.K. Mishra, Effect of nitrogen on mechanical, oxidation and structural behaviour of Ti–Si–B–C–N nanocomposite hard coatings deposited by DC sputtering, Surf. Interface Anal. 48 (2016) 1080–1089, https://doi.org/10.1002/sia.6030.
[31] F. Vaz, J. Ferreira, E. Ribeiro, L. Rebouta, S. Lanceros-Méndez, J.A. Mendes, E. Alves, P. Goudeau, J.P. Rivière, F. Ribeiro, I. Moutinho, K. Pischow, J. de Rijk, Influence of nitrogen content on the structural, mechanical and electrical properties of TiN thin films, Surf. Coat. Technol. 191 (2005) 317–323, https://doi.org/10.1016/j.surfcoat.2004.01.033.
[32] H.A. Macías, L. Yate, L.E. Coy, J.J. Olaya, W. Aperador, Effect of nitrogen flow ratio on microstructure, mechanical and tribological properties of TiWSiNx thin film deposited by magnetron co-sputtering, Appl. Surf. Sci. 456 (2018) 445–456, https://doi.org/10.1016/j.apsusc.2018.06.129.
[33] S. Logothetidis, E.I. Meletis, G. Stergioudis, A.A. Adjaottor, Room temperature oxidation behavior of TiN thin films, Thin Solid Films 338 (1999) 304–313, https://doi.org/10.1016/S0040-6090(98)00975-4.
[34] Thomas C. Allison, NIST-JANAF Thermochemical Tables - SRD 13, National Institute of Standards and Technology, 2013.
[35] P.-C. Tsai, W.-J. Chen, J.-H. Chen, C.-L. Chang, Deposition and characterization of TiBCN films by cathodic arc plasma evaporation, Thin Solid Films 517 (2009) 5044–5049, https://doi.org/10.1016/j.tsf.2009.03.029.
[36] W. Gissler, Structure and properties of Ti-B-N coatings, Surf. Coat. Technol. 68-69 (1994) 556–563, https://doi.org/10.1016/0257-8972(94)90217-8.
[37] I. Asempah, J. Xu, L. Yu, H. Ju, F. Wu, H. Luo, Microstructure, mechanical and tribological properties of magnetron sputtered Ti-B-N films, Surf. Eng. 35 (2019) 701–709, https://doi.org/10.1080/02670844.2019.1575569.
[38] Y.H. Cheng, T. Browne, B. Heckerman, Influence of CH4 fraction on the composition, structure, and internal stress of the TiCN coatings deposited by LAFAD technique, Vacuum 85 (2010) 89–94, https://doi.org/10.1016/j.vacuum.2010.04.007.
[39] H. Xu, X. Nie, R. Wei, Tribological behavior of a TiSiCN coating tested in air and coolant, Surf. Coat. Technol. 201 (2006) 4236–4241, https://doi.org/10.1016/j.surfcoat.2006.08.066.
[40] S. Ghasemi, A.R. Farhadizadeh, A.A. Amadeh, H. Ghomi, Structural and morphological properties of TiN deposited by magnetron sputtering, Surf. Topogr.: Metrol. Prop. 6 (2018) 45003, https://doi.org/10.1088/2051-672X/aae405.
[41] H. Hetzner, C. Schmid, S. Tremmel, K. Durst, S. Wartzack, Empirical-statistical study on the relationship between deposition parameters, process variables, deposition rate and mechanical properties of a-C:H:W coatings, Coatings 4 (2014) 772–795, https://doi.org/10.3390/coatings4040772.
[42] A.R. Nyaiesh, L. Holland, The dependence of deposition rate on power input for dc and rf magnetron sputtering, Vacuum 31 (1981) 315–317, https://doi.org/10.1016/S0042-207X(81)80503-9.
[43] S. Zhang, D. Sun, Y. Fu, H. Du, Q. Zhang, Effect of sputtering target power density on topography and residual stress during growth of nanocomposite nc-TiN/a-SiNx thin films, Diam. Relat. Mater. 13 (2004) 1777–1784, https://doi.org/10.1016/j.diamond.2004.03.008.
[44] Y.H. Lu, Y.G. Shen, Z.F. Zhou, K.Y. Li, Phase configuration, nanostructure evolution, and mechanical properties of unbalanced magnetron-sputtered Ti-Cx-Ny thin films, J. Vac. Sci. Technol. A 25 (2007) 1539–1546, https://doi.org/10.1116/1.2784719.
[45] T. Fu, Z.F. Zhou, K.Y. Li, Y.G. Shen, Structure, stress and hardness of sputter deposited nanocomposite W-Si-N coatings, Surf. Coat. Technol. 200 (2005) 2525–2530, https://doi.org/10.1016/j.surfcoat.2005.04.024.
[46] H.L. Liu, C.Z. Huang, J. Wang, J. Sun, Microstructure and mechanical properties of two kinds of Al_2O_3/SiC nanocomposites, MSF 471-472 (2004) 243–247, https://doi.org/10.4028/www.scientific.net/MSF.471-472.243.
[47] A. Sanaty-Zadeh, Comparison between current models for the strength of particulate-reinforced metal matrix nanocomposites with emphasis on consideration of Hall–Petch effect, Mater. Sci. Eng. A 531 (2012) 112–118, https://doi.org/10.1016/j.msea.2011.10.043.
[48] L. Karlsson, L. Hultman, J.-E. Sundgren, Influence of residual stresses on the mechanical properties of TiCxN1–x (x=0, 0.15, 0.45) thin films deposited by arc evaporation, Thin Solid Films 371 (2000) 167–177, https://doi.org/10.1016/S0040-6090(00)00996-2.
[49] H. Oettel, R. Wiedemann, S. Preißler, Residual stresses in nitride hard coatings prepared by magnetron sputtering and arc evaporation, Surf. Coat. Technol. 74-75 (1995) 273–278, https://doi.org/10.1016/0257-8972(95)08235-2.
[50] J. Houska, O. Warschkow, M.M.M. Bilek, D.R. McKenzie, J. Vlcek, S. Potocky, The effect of argon on the structure of amorphous SiBCN materials: an experimental and ab initio study, J. Phys. Condens. Matter 18 (2006) 2337–2348, https://doi.org/10.1088/0953-8984/18/7/019.
[51] M. Dildrop, Entwicklung kombinierter Schichtsysteme für thermomechanisch hochbelastete Werkzeuge. Dissertation.
[52] C.-L. Chang, T.-J. Hsieh, Effect of C2H2 gas flow rate on synthesis and characteristics of Ti–Si–C–N coating by cathodic arc plasma evaporation, J. Mater. Process. Technol. 209 (2009) 5521–5526, https://doi.org/10.1016/j.jmatprotec.2009.05.008.
[53] S. Ma, J. Procházka, P. Karvánková, Q. Ma, X. Niu, X. Wang, D. Ma, K. Xu, S. Vepřek, Comparative study of the tribological behaviour of superhard nanocomposite coatings nc-TiN/a-Si3N4 with TiN, Surf. Coat. Technol. 194 (2005) 143–148, https://doi.org/10.1016/j.surfcoat.2004.05.007.
[54] F. Cao, P. Munroe, Z. Zhou, Z. Xie, Mechanically robust TiAlSiN coatings prepared by pulsed-DC magnetron sputtering system: scratch response and tribological performance, Thin Solid Films 645 (2018) 222–230, https://doi.org/10.1016/j.tsf.2017.10.058.
[55] M.A. Hassan, A.R. Bushroa, R. Mahmoodian, Identification of critical load for scratch adhesion strength of nitride-based thin films using wavelet analysis and a proposed analytical model, Surf. Coat. Technol. 277 (2015) 216–221, https://doi.org/10.1016/j.surfcoat.2015.07.061.
[56] F. Li, S. Zhang, J. Kong, Y. Zhang, W. Zhang, Multilayer DLC coatings via alternating bias during magnetron sputtering, Thin Solid Films 519 (2011) 4910–4916, https://doi.org/10.1016/j.tsf.2011.01.052.
[57] S.J. Bull, Failure mode maps in the thin film scratch adhesion test, Tribol. Int. 30 (1997) 491–498, https://doi.org/10.1016/S0301-679X(97)00012-1.
[58] A. Lahmar, A. Assaf, M.J. Durand, S. Jouanneau, G. Thouand, B. Garnier, Factors influencing adhesion of submicrometer thin metal films: critical review, Rev. Adhes. Adhesives 4 (2016) 47–68, https://doi.org/10.7569/RAA.2016.097301.
[59] S. PalDey, S. Deevi, Single layer and multilayer wear resistant coatings of (Ti,Al)N: a review, Mater. Sci. Eng. A 342 (2003) 58–79, https://doi.org/10.1016/S0921-5093(02)00259-9.
[60] P.A. Steinmann, Y. Tardy, H.E. Hintermann, Adhesion testing by the scratch test method: the influence of intrinsic and extrinsic parameters on the critical load, Thin Solid Films 154 (1987) 333–349, https://doi.org/10.1016/0040-6090(87)90377-4.
[61] Y.H. Lu, Y.G. Shen, Z.F. Zhou, K.Y. Li, Effects of B content and wear parameters on dry sliding wear behaviors of nanocomposite Ti–B–N thin films, Wear 262 (2007) 1372–1379, https://doi.org/10.1016/j.wear.2007.01.024.
[62] D. Ma, S. Ma, H. Dong, K. Xu, T. Bell, Microstructure and tribological behaviour of super-hard Ti–Si–C–N nanocomposite coatings deposited by plasma enhanced chemical vapour deposition, Thin Solid Films 496 (2006) 438–444, https://doi.org/10.1016/j.tsf.2005.08.379.
[63] J.C. Caicedo, E. Hernandez-Rengifo, C. Ortíz, L.A. Rodríguez, C. Magén, Tribomechanical analysis and machining development for TiSiCN material deposited on industrial steel, Int J Adv Manuf Technol 128 (2023) 5437–5461. https://doi.org/10.1007/s00170-023-11966-1.